PROCEEDINGS A

royalsocietypublishing.org/journal/rspa

Research

Cite this article: Kothari M, Cha M-H, Lefevre V, Kim K-S. 2019 Critical curvature localization in graphene. II. Non-local flexoelectricity–dielectricity coupling. *Proc. R. Soc. A* **475**: 20180671.
http://dx.doi.org/10.1098/rspa.2018.0671

Received: 26 September 2018
Accepted: 18 December 2018

Subject Areas:
nanotechnology, mechanics, atomic and molecular physics

Keywords:
graphene crinkle, non-local flexoelectricity, flexoelectricity–dielectricity coupling, surface-charge concentration, molecular adsorption, thermodynamic framework

Author for correspondence:
Kyung-Suk Kim
e-mail: kyung-suk_kim@brown.edu

†Present address: Samsung Electronics, Kiheung, Korea.
‡Present address: Department of Mechanical Engineering, Northwestern University, Evanston, IL 60208.

THE ROYAL SOCIETY PUBLISHING

Critical curvature localization in graphene. II. Non-local flexoelectricity–dielectricity coupling

Mrityunjay Kothari, Moon-Hyun Cha†, Victor Lefevre‡ and Kyung-Suk Kim

School of Engineering, Brown University, Providence, RI 02912, USA

K-SK, 0000-0003-0681-346X

As a sequel of part I (Kothari *et al*. 2018 *Proc. R. Soc. A* **474**, 20180054), we present a general thermodynamic framework of flexoelectric constitutive laws for multi-layered graphene (MLG), and apply these laws to explain the role of crinkles in peculiar molecular adsorption characteristics of highly oriented pyrolytic graphite (HOPG) surfaces. The thermodynamically consistent constitutive laws lead to a non-local interaction model of polarization induced by electromechanical deformation with flexoelectricity–dielectricity coupling. The non-local model predicts curvature and polarization localization along crinkle valleys and ridges very close to those calculated by density functional theory (DFT). Our analysis reveals that the non-local model can be reduced to a simplified uc-local or e-local model (Kothari *et al*. 2018 *Proc. R. Soc. A* **474**, 20180054) only when the curvature distribution is uniform or highly localized. For the non-local model, we calibrated and formulated the layer-number-dependent dielectric and intrinsic flexoelectric coefficients of MLGs. In addition, we also obtained layer-number dependent flexoelectric coefficients for uc-local and e-local models. Our DFT analysis shows that polarization-induced adsorption of neutral molecules at crinkle ridges depends on the molecular weight of the molecule. Furthermore, our detailed study of polarization localization in graphene crinkles enables us to understand previously unexplained self-organized adsorption of C_{60} buckyballs in a linear array on an HOPG surface.

1. Introduction

This paper is a sequel of Critical curvature localization in graphene. I. Quantum flexoelectricity effect [1].

In part I, we used a specific constitutive relation, *e-local model*, for flexoelectricity of graphene to understand a peculiar localization mode, crinkle, in graphene. Here, our interest is in the self-consistent description of flexoelectricity in multi-layered structures in the context of coupling between flexoelectricity and dielectricity for general two-dimensional layered materials, and extraction of associated material properties from DFT calculations. To this end, in the current work, we derive an appropriate free-energy potential for flexoelectric modelling consistent with the thermodynamic framework and apply such framework for modelling electromechanical deformation of two-dimensional layered materials with a field-of-view resolution in nanometre scale. As a consequence, we can characterize and control not only flexoelectric polarizations but also Fermi and Landau levels near crinkle ridges where the layers are highly curved, as well as over flat wings of the crinkles where layer stacking is uniformly sheared. Discovery, characterization and control of crinkles in emerging two-dimensional materials are expected to open up diverse applications in electronics and photonics, and biology and medicine through self-assembly and pattern control of novel nanostructures [2,3].

Some of the early theoretical studies on flexoelectricity of crystals was reported by Mashkevich [4] and Kogan [5]. A phenomenological constitutive law was postulated by Kogan [5] for bulk polarization density, P_i, in non-piezoelectric materials,

$$P_i = \chi_{ij} E_j + \beta_{ijkl} (\nabla \varepsilon)_{jkl}, \tag{1.1}$$

where χ_{ij} represents electric susceptibility tensor, E_j electric field, β_{ijkl} flexoelectricity tensor and $(\nabla \varepsilon)_{jkl}$ strain gradient. In more recent works on continuum modelling of flexoelectricity and general electromechanical formulation [6–9], the constitutive relation is derived in a context of internal free energy ($\mathcal{F}$) formulation. In their work, the total internal free energy is described as a functional of displacement, $\boldsymbol{u}$, the bulk polarization density, $\boldsymbol{P}$ and the scalar electric potential, ξ, as

$$\mathcal{F}[\boldsymbol{u}, \boldsymbol{P}] = \int_{\Omega} W[\boldsymbol{u}, \boldsymbol{P}] \, \mathrm{d}\Omega + \int_{\mathbb{R}^3} \frac{\epsilon_0}{2} |\nabla \xi|^2 \, \mathrm{d}V, \tag{1.2}$$

where W represents a free-energy density defined only in the volume of the material Ω in the deformed configuration, while $\mathbb{R}^3$ denotes the entire space.

In the absence of free charges, (1.2) can be further reduced to a thermodynamically consistent constitutive relation of a *local differential-type material behaviour*. Then, the internal energy per unit volume, U, is expressed in terms of fundamental work-conjugate displacement variables—strain, strain gradient and electric displacement, $\{\boldsymbol{\varepsilon}, \nabla \boldsymbol{\varepsilon}, \mathbf{D}\}$—of stress, couple stress and the electric field, $\{\boldsymbol{\sigma}, \boldsymbol{m}, \boldsymbol{E}\}$. The internal energy is explicitly expressed as

$$\int_{\mathbb{R}^3} U(\boldsymbol{\varepsilon}, \nabla \boldsymbol{\varepsilon}, \mathbf{D}) \, \mathrm{d}V = \int_{\Omega} \int_0^{\boldsymbol{\varepsilon}} \boldsymbol{\sigma} d\boldsymbol{\varepsilon} \, \mathrm{d}\Omega + \int_{\Omega} \int_0^{\nabla \boldsymbol{\varepsilon}} \boldsymbol{m} d \nabla \boldsymbol{\varepsilon} \, \mathrm{d}\Omega + \int_{\mathbb{R}^3} \int_0^{D} \boldsymbol{E} d\mathbf{D} \, \mathrm{d}V, \tag{1.3}$$

where all the products on the right-hand side are scalar products. Then, this expression leads to constitutive relations,

$$\boldsymbol{\tau}(\boldsymbol{\varepsilon}, \nabla \boldsymbol{\varepsilon}, \mathbf{D}) = \frac{\partial U}{\partial \boldsymbol{\eta}}, \tag{1.4}$$

where $\boldsymbol{\tau}$ represents the set of variables $\{\boldsymbol{\sigma}, \boldsymbol{m}, \boldsymbol{E}\}$ and $\boldsymbol{\eta}$ the set $\{\boldsymbol{\varepsilon}, \nabla \boldsymbol{\varepsilon}, \mathbf{D}\}$. In the *linear-response range of the constitutive relation*, (1.4), the internal energy has a quadratic form,

$$U = \frac{1}{2} \boldsymbol{\eta} \cdot \boldsymbol{Q} \cdot \boldsymbol{\eta}, \tag{1.5}$$

where $\boldsymbol{Q}$ represents symmetric electromechanical-property coefficients. $\boldsymbol{Q}$ comprises six sets of material properties in the most general case. For a non-piezoelectric material, ignoring the strain-gradient effect on mechanical stress, the coefficient set $\boldsymbol{Q}$ reduces to four sets that correspond to stress/strain stiffness, couple-stress/strain-gradient stiffness, inverse electric permittivity and flexoelectric coefficients, respectively. However, the total number of coefficients in $\boldsymbol{Q}$ is too large to be practical for measurement in highly anisotropic materials and/or two-dimensional layered materials. On the other hand, when we consider deformation of a two-dimensional

layered structure like multilayer graphene (MLG), the electromechanical deformation is primarily composed of distinct modes, such as interlayer shear and individual layer bending, and often localizes at a narrow band of nanometre-scale width. Therefore, it is more practical to treat the internal energy as those of individual layers described with the framework of (1.5) and those of interlayer deformation.

For modelling developable deformation mode of two-dimensional layered structures, the stretch is decoupled from bending in the internal energy per unit area of the individual layer, $U_{(L)}$. The decoupling reduces $\boldsymbol{Q}$ to its two-dimensional analogue $\boldsymbol{Q}_{(2D)}$, leading to four coefficients for developable deformation:

$$U_{(L)}[\varepsilon,\kappa,D]=\frac{1}{2}Y^{(D)}\varepsilon^2+\frac{1}{2}Q_b^{(D)}\kappa^2+\beta^{(D)}\kappa D+\frac{1}{2\epsilon^{(D)}}D^2, \tag{1.6}$$

where, ε denotes the stretching strain and κ the curvature of the layer, while $Y^{(D)}, Q_b^{(D)}, \beta^{(D)}$ and $1/\epsilon^{(D)}$ are the components of $\boldsymbol{Q}_{(2D)}$. Employing *Legendre transform* [10] for variable change from D to P, and noting that $D=\varepsilon_0 E+P$, we define a new free-energy potential $\phi_{(L)}\equiv\phi_{(L)}[\varepsilon,\kappa,P]$. The transformation enables us to exclude the domain integral over $\mathbb{R}^3\backslash\Omega$ in evaluating the total free energy of the system with the vanishing electric field at infinity, which makes computational analysis simpler. The transformed free-energy potential is expressed as

$$\phi_{(L)}[\varepsilon,\kappa,P]=U_{(L)}[\varepsilon,\kappa,D]-\frac{\epsilon_0}{2}E^2=\frac{1}{2}Y^{(P)}\varepsilon^2+\frac{1}{2}Q_b^{(P)}\kappa^2+\beta^{(P)}\kappa P+\frac{1}{2\chi^{(P)}}P^2, \tag{1.7a}$$

and the corresponding constitutive relations are given by (1.4) to have

$$\left\{\sigma=Y^{(P)}\varepsilon, m=Q_b^{(P)}\kappa+\beta^{(P)}P, E=\beta^{(P)}\kappa+\frac{1}{\chi^{(P)}}P\right\}, \tag{1.7b}$$

where $Y^{(P)}, Q_b^{(P)}, \beta^{(P)}$ and $1/\chi^{(P)}$ are the coefficients for $\{\varepsilon,\kappa,P\}$-based description.

Specializing for the case of graphene, we employ inextensibility of the layer as a limiting approximation which drops ε-dependence of $\phi_{(L)}$ and σ in (1.7*a* and *b*), and rearrange (1.7*b*–3) to get

$$\overset{\vee}{P}=\alpha\overset{\vee}{E}+\beta\kappa. \tag{1.8}$$

Here $\overset{\vee}{()}$ denotes the component normal to graphene layer, $\overset{\vee}{P}$ the polarization density per unit area, α the two-dimensional atomic-layer polarizability of graphene, $\overset{\vee}{E}$ the point exclusive electric field that includes the field generated by polarization elsewhere and $\beta=-\beta^{(P)}\chi^{(P)}$ the two-dimensional flexoelectric coefficient. The point exclusive description of $\overset{\vee}{E}$ in (1.8) represents non-local flexoelectricity–dielectricity coupling in graphene. For the rest of the paper, we make use of (1.8) as the constitutive law of non-local flexoelectric polarization coupled with dielectric polarization. However, this formulation makes the polarization-induced electric field singular, and the singularity is typically regulated by the cut-off radius technique discussed in [1,11]. Note that while Clausius–Mossotti relationship expresses the electric susceptibility, χ, of a material in terms of the atomic polarizability, α^*, of the constituent atoms for a bulk formulation, for modelling two-dimensional layered materials like graphene, we employ (1.8) in terms of atomic-layer polarizability per unit area, α.

The organization of the paper is as follows: in §2, we discuss the reduced models of flexoelectricity and the importance of flexoelectricity–dielectricity coupling. The analysis of the non-local model is presented in §3 followed by DFT studies on adsorption of molecules on crinkles in §4. We discuss the implications of the non-locality in §5 and subsequently conclude by summarizing and proposing future directions in §6.

2. Flexoelectricity models

As aforementioned, in this paper, we focus on flexoelectricity in MLG. We recently reported [1,12] the discovery of a new subcritical buckling mode of MLG which shows high curvature

localization. DFT studies indicated that the curvature of the crinkle mode remains focused in a very narrow band of width 0.86 nm which remains fixed even as the amplitude of the mode increases. There, a reduced model of flexoelectricity that lumps together the flexoelectric and dielectric effects was presented. The model predicted crinkle formation with peak curvatures approximately $0.15\,\mathrm{nm}^{-1}$ and peak polarization density approximately $0.11\mathrm{e}\,\mathrm{nm}^{-1}$ for a 3° end angle, leading to a concentration of static electric charges at the crinkle ridges and valleys on the free surface. However, the peak polarization density was found to be significantly higher than that predicted by the single-layer flexoelectric constant of uniform curvature [13]. In order to address the apparent multitude of flexoelectric constants, we develop a model including flexoelectricity–dielectricity coupling consistent with the thermodynamic framework. This model is inherently non-local because the flexoelectric and dielectric polarization interact and influence each other. In this section, we discuss two reduced models of quantum flexoelectricity in graphene and lay the background for a general model.

(a) Reduced constitutive models of flexoelectricity

Figure 1*a*(i) depicts the configuration (grey curve), curvature distribution (solid line) and polarization distribution (dash-dot line) in a uniformly bent graphene layer. The polarization is proportional to curvature, and the proportionality constant is called the two-dimensional *uniform curvature flexoelectric constant* $\beta^{(uc)}$. Kalinin & Meunier [13] evaluated $\beta^{(\mathrm{uc})}_{(1)} \approx 0.11\mathrm{e}$ with first-principle calculations, naming it as a quantum flexoelectric coefficient, for

$$\overset{\vee}{P} = \beta^{(\mathrm{uc})}_{(1)}\kappa, \tag{2.1}$$

where the subscript of $\beta^{(\mathrm{uc})}_{(1)}$ indicates a single layer. Here, we call (2.1) the uc-local model.

On the other hand, for a much more complex non-uniform bending, the above model falls short. Figure 1*a*(ii) illustrates non-uniform distributions of configuration, curvature and polarization near a crinkle ridge, indicating that polarization is under-predicted by the uc-local model. Calibration with the DFT analysis of crinkles [1] yields an effective flexoelectric constant of an MLG crinkle ridge as $\beta^{*}_{(21)} = 0.759e$, which is 6.9 times $\beta^{(\mathrm{uc})}_{(1)}$, for

$$\overset{\vee}{P} = \beta^{*}\kappa. \tag{2.2}$$

Here, $\beta^{*}_{(21)}$ stands for average flexoelectric constant of an individual layer in 21-layer graphene for modelling with an inextensible-layer limit. In part I [1], we employed the reduced model (2.2) without explicit involvement of dielectric constant α like in (1.8). The lumping of the inherent non-locality in the flexoelectricity–dielectricity coupling into a local constitutive relationship is exact for uniform curvature distribution while it is an approximation for the crinkle problem. However, in general, the reduced models *do not* work for an arbitrary non-uniform curvature distribution and therefore, a more detailed explicit treatment of dielectricity is undertaken in the following sections.

(b) Flexoelectricity–dielectricity coupling

MLG is anisotropic in its response to electric field. It acts as an in-plane conductor at finite temperature and as a dielectric in the direction normal to the lattice layer. A full treatment of flexoelectricity for general curvature distribution involves long range dipole–dipole interactions through electric fields generated by the polarization distribution, leading to flexoelectricity–dielectricity coupling in the normal direction (1.8).

Figure 1*b*(i–iv) illustrate flexoelectricity–dielectricity coupling mechanisms in dipole–dipole interactions near a crinkle ridge of MLG, based on the curvature distribution obtained by DFT in [1]. Figure 1*b*(i) shows the net polarization (blue arrows) developed in a crinkle boundary layer. Owing to curvature reversal, we get regions of positive and negative net polarization. This picture does not take into account any dielectric interactions explicitly. To uncouple flexoelectricity and

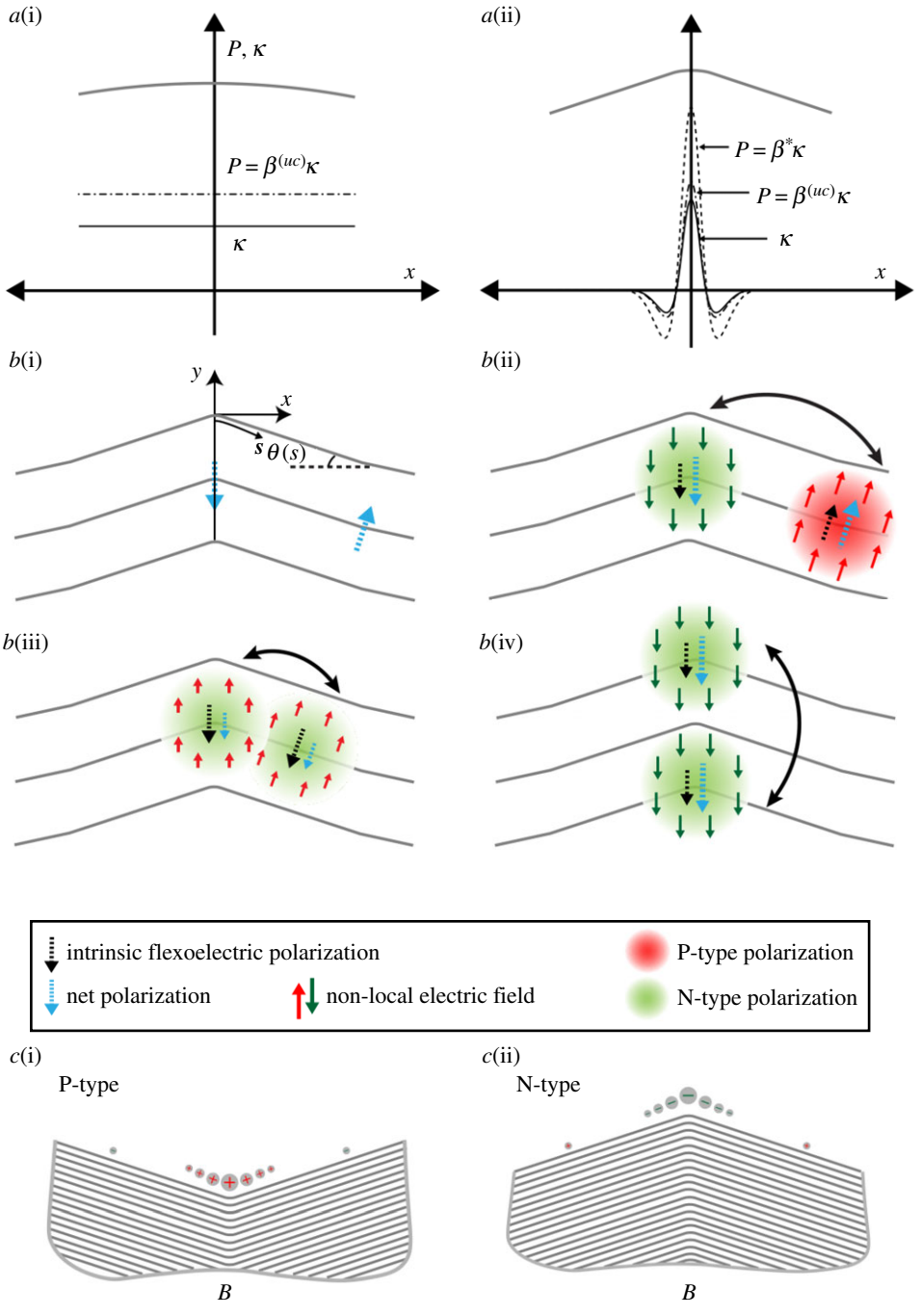

Figure 1. (*a*(i)) Polarization distribution for a uniform curvature case; (ii) polarization distribution for a crinkle curvature distribution; (*b*(i)) overall picture of the polarization on the layer, curvature reversal causes polarization reversal; (ii) in the intralayer case, electric fields amplify the anti-parallel polarization and (iii) diminish the parallel polarization; (iv) interlayer interactions amplify the parallel polarization.

dielectricity effects, we show the intrinsic flexoelectric polarization and the associated electric fields in figure 1*b*(ii). Bending of graphene creates a curvature which breaks the symmetry in the electron cloud distribution in graphene. This separation of positive and negative charge centres

in graphene produces a polarization, which we refer to as the intrinsic flexoelectric polarization (black arrows). The intrinsic polarization thus developed, produce electric fields which influence the polarization in their neighbourhood—either amplifying it (figure 1*b*(ii)) or weakening it (figure 1*b*(iii)). The combined effect leads to the net polarization. As illustrated for the intralayer case, the interlayer interactions follow a similar interaction mechanism (figure 1*b*(iv)). Note that the size of the blue arrow is larger than a black arrow in figure 1*b*(ii) and smaller in figure 1*b*(iii), indicating the amplifying and weakening effects, respectively. Within the layer, anti-parallel dipoles reinforce each other because the additional dielectric polarization points in the same direction as the intrinsic flexoelectric polarization. By contrast, the parallel dipoles weaken each other because the dielectric polarization points opposite to the intrinsic flexoelectric polarization. Similarly, in figure 1*b*(iv), the blue arrows are larger because parallel dipoles reinforce each other in the interlayer setting. This is why crinkles, because of the signature curvature reversal, show a much larger $\beta^{*}_{(21)}$ in comparison to $\beta^{(\mathrm{uc})}_{(1)}$. Depending on the parity of bending, the flexoelectric charges developed on the surface can be positive or negative, as illustrated in figure 1*c*(i,ii). Following the nomenclature introduced in [12], the positively charged crinkle is called P-type and the negatively charged, N-type crinkle.

3. Analysis of the non-local flexoelectric model

(a) Formulation

In this section, we employ the non-local flexoelectricity–dielectricity coupling in the buckling and post-buckling analysis of suspended MLG in a plane-strain setting. We consider the set-up in [1], with N-layer MLG, interlayer spacing $a = 0.34$ nm and total length $2L_0$. The bending stiffness of each layer in the {κ, P}-based description is denoted as $Q_b^{(P)}$ and the interlayer shear modulus is μ. For the nano-structural model, we make use of DFT-evaluated material properties, $Q_b^{(P)} = 1.0$eV [14], and $\mu = 4$ GPa [15]. The atomic polarizability of graphene is reported in the literature to be $\alpha^{*} \sim 0.85$ Å^3 [16,17]. Following the same kinematic assumptions as [1], the layers deform identically and are inextensible. Under these assumptions, the total free-energy potential Φ as defined in (1.7*a*), can be given as the sum of mechanical and electrostatic parts. The mechanical part, Φ_{mech}, has two contributions, namely the bending of individual layers and interlayer shear.

$$\Phi_{\mathrm{mech}} = \int_{-L_0}^{L_0} \left(\frac{Q_b^{(P)} N}{2} \left(\frac{d\theta}{ds} \right)^2 + \frac{\mu (N-1) a}{2} \tan^2 \theta \right) \mathrm{d}s, \tag{3.1}$$

where $\theta(s)$ is the slope angle and $\kappa = d\theta/ds$ is the curvature of the layer.

The electrostatic part, Φ_{elec}, is given as

$$\Phi_{\mathrm{elec}} = \frac{-1}{2\pi \epsilon_{(N)}} \sum_{n=1}^{N} \sum_{m=1}^{n} \int \int_{-L_0}^{L_0} \overset{\vee}{P}(s_n) \overset{\vee}{P}(s'_m) \frac{\{1 - \delta_{mn} q_2(s_n, s'_n)\} \{\mathrm{A}(s_n, s'_m) + \mathrm{B}(s_n, s'_m)\}}{[\{x(s_n) - x(s'_m)\}^2 + \{y(s_n) - y(s'_m)\}^2]^2} \mathrm{d}s_n \mathrm{d}s'_m, \tag{3.2a}$$

$$\begin{aligned} A(s_n, s'_m) &= \cos\{\theta(s_n) + \theta(s'_m)\} [-\{x(s_n) - x(s'_m)\}^2 + \{y(s_n) - y(s'_m)\}^2] \\ \mathrm{B}(s_n, s'_m) &= 2\sin\{\theta(s_n) + \theta(s'_m)\} \cdot \{x(s_n) - x(s'_m)\} \{y(s_n) - y(s'_m)\}, \end{aligned} \tag{3.2b}$$

$$q_2(s_n, s'_n) = \begin{cases} \frac{1}{2}, & \text{for } |s_n - s'_n| > r_0 \\ 1, & \text{for } |s_n - s'_n| \le r_0 \end{cases}, \tag{3.2c}$$

where r_0 is the cut-off radius of the interaction integration and m, n are indices for the layers whose interaction is being counted.

The electric field, $\overset{\vee}{E}$, resulting from any arbitrary polarization distribution, $\overset{\vee}{P}$, over N layers of graphene can be expressed as a linear operation on polarization,

$$\overset{\vee}{E}(s'_m) = \frac{1}{2\pi\epsilon_{(N)}} \sum_{n=1}^{N} \int_{-L_0}^{L_0} \overset{\vee}{P}(s_n) \frac{\{1-\delta_{mn} q(s_n, s'_n)\}\{A(s_n, s'_m) + B(s_n, s'_m)\}}{[\{x(s_n) - x(s'_m)\}^2 + \{y(s_n) - y(s'_m)\}^2]^2} \mathrm{d}s_n, \tag{3.3a}$$

$$\begin{aligned} A(s_n, s'_m) &= \cos\{\theta(s_n) + \theta(s'_m)\}[-\{x(s_n) - x(s'_m)\}^2 + \{y(s_n) - y(s'_m)\}^2] \\ \mathrm{B}(s_n, s'_m) &= 2\sin\{\theta(s_n) + \theta(s'_m)\} \cdot \{x(s_n) - x(s'_m)\}\{y(s_n) - y(s'_m)\}, \end{aligned} \tag{3.3b}$$

and

$$q_1(s_j, s'_j) = \begin{cases} 0, & \text{for } |s_j - s'_j| > r_0 \\ 1, & \text{for } |s_j - s'_j| \le r_0 \end{cases}, \tag{3.3c}$$

where s is the arclength parameter, $\theta(s)$ the slope angle of the layers, m the index of the layer where the electric field is being calculated, r_0 the cut-off radius and index n sums over all the layers. Combining (3.3a) with the non-local constitutive relation (1.8), we express $\overset{\vee}{P}$ as a function of the shape of the layer as

$$\mathcal{L}_2[\overset{\vee}{P}] = \beta\kappa, \tag{3.4}$$

where $\mathcal{L}_2$ is a linear operator.

Thus, (3.1), (3.2) and (3.4) complete the formulation of the minimization problem in terms of total potential energy $\Pi[\theta]$ where

$$\Pi[\theta] = \Phi_{\mathrm{mech}} + \Phi_{\mathrm{elec}} - \int_{-L_0}^{L_0} f(1 - \cos\theta)\, \mathrm{d}s, \tag{3.5}$$

and f is the constraint force necessary to maintain the configuration. The functional $\Pi[\theta(s)]$ can then be numerically minimized to obtain the post-buckling configuration of MLG. Figure 2 shows the collection of results for a 21-layer, 15 nm long MLG. Cut-off radius for the calculation, r_0, was chosen to be 0.14 nm which is approximately the same as the lattice parameter of graphene. The intrinsic flexoelectric constant was obtained by calibration of a numerical model with DFT. This calibration was done by best fitting a single case ($\theta_e = 3^\circ$) to the DFT results of [1]. The value of intrinsic flexoelectric constant, $\beta^{(\mathrm{in})}_{(21)}$, was obtained to be approximately 0.733e.

Comparison of peak curvatures predicted by the non-local model to DFT results in figure 2*a*(i) shows a good agreement for different end angles. In the post-buckling evolution, the crinkle mode shape is found to remain the same while the amplitude increases with the end angle, thus explaining the observed linear trend in the peak curvatures. Figure 2*a*(i) inset shows the localized curvature distribution with the fast-decaying oscillating tail. The distance between the closest inflection points on either side of origin is treated as a measure of localization—*the curvature focusing band width*—and it is found to be approximately 0.86 nm, agreeing well with the DFT findings. Figure 2*a*(ii) shows the peak polarization density comparison between the uc-local model and the non-local flexoelectric model. As explained in §2a and §2b, the uc-local model is found to severely under-predict the peak curvature compared with the non-local model which predicts about 6.9 times higher peak polarization values than the uc-local model. This remarkable difference between the two models is due to the inadequacy of the uc-local model in accounting for flexoelectricity–dielectricity coupling. The inset shows the distribution of polarization density for three different end angles. The mode shape of the polarization distribution nearly remains the same and is only scaled by the amplitude that is dependent on the end angle practically in a linear fashion.

(b) Effect of dielectricity

Figure 2*b*(i,ii) highlights the difference between e-local model and non-local model results. As discussed in the §2b, for a localized and oscillating curvature distribution, the flexoelectric–dielectric coupling reinforces the curvature peaks and valley, amplifying the polarization. Thus,

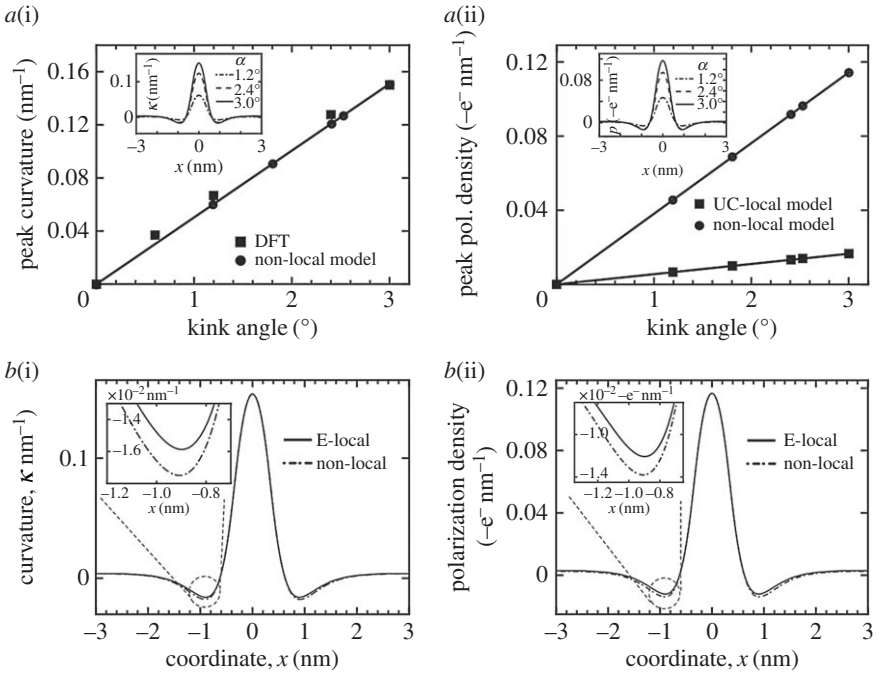

Figure 2. (*a*(i)) Peak curvature comparison between non-local model and DFT results; ((i) inset) curvature distribution for 21-layer 15 nm sample; (ii) peak polarization density comparison between non-local and uc-local model; ((ii) inset) polarization density distribution for 21-layer 15 nm sample; (*b*(i)) Comparison between e-local and non-local model curvature distribution and (ii) polarization density distribution highlighting the differences.

in order to understand the difference between the e-local model and non-local model, we look closely at the curvature valley in figure 2*b*(i) (inset shows the blown-up view). The non-local model has deeper curvature valley because the oscillating polarization in the neighbouring regions contributes to amplify the net polarization which further enhances curvature localization. The peak curvatures of the non-local model are calibrated to match the peak curvatures of DFT results, so they do not show this variation at the peak. Similarly, the figure 2*b*(ii) shows the deeper valleys in polarization plot. This deeper polarization reversal provides an even lower energetic state due to attractive interactions between the dipoles. The e-local model, due to the lumping of dielectric and flexoelectric effects into a single term, misses out on this detail. The difference between the e-local model and non-local model is subtle here, as it should be, because the e-local model has been shown to work well for modelling crinkles. However, for modelling a general non-uniform curvature distribution, the reduced models—uc-local and the e-local model—may not work well and the non-local model must be applied.

4. Flexoelectric polarization and molecular adsorption

Figure 3*a*(i) shows a comparison between polarization distributions predicted by the non-local model and the DFT analysis. The comparison is made through width-dependent mean polarization density, $\bar{P}(x)$, near a crinkle ridge up to 4 nm width. Here, $\bar{P}(x)$ is defined as

$$\bar{P}(x) = \frac{1}{2x}\int_{-x}^{x} P(\xi)\,\mathrm{d}\xi, \tag{4.1}$$

where $P(\xi)$ is the polarization density at ξ measured from the maximum or minimum point of polarization for a crinkle valley or a ridge, respectively. For the cases considered for comparison—1.8° and 3° end angle of the crinkle—we find good agreement between the DFT and the non-local

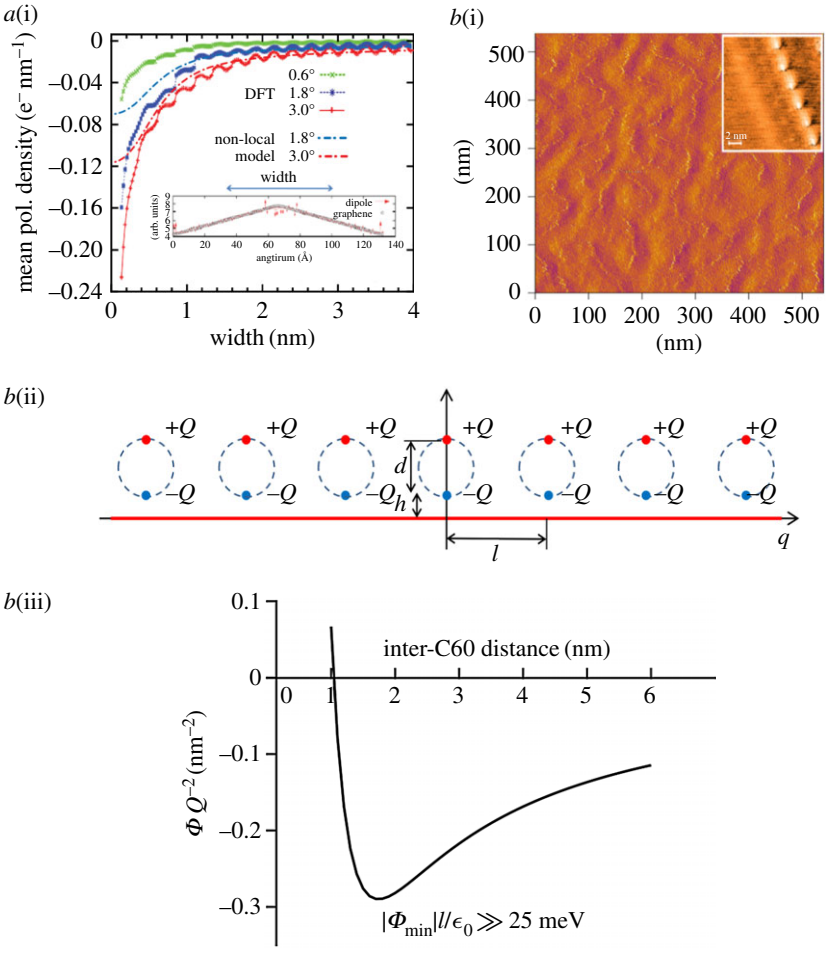

Figure 3. (*a*) Mean polarization density comparison between non-local model and DFT results; (*b*(i)) Buckyball adsorption on HOPG [12]; ((i) inset) higher resolution image showing the periodicity of buckyballs on HOPG [18]; (ii) Schematic of buckyballs on crinkle ridge; (iii) Potential energy of the system as a function of inter-buckyball spacing *l*.

model results for most of the width of averaging, x, except for x close to cut-off radius, as expected. The continuum model interpretation starts to break down for x comparable to the cut-off radius. The peculiar oscillations seen in the DFT mean polarization density can be attributed to the averaging scheme of polarization with the reciprocal space wave function for x in the real space not aligned with periodic atomic locations with the Bader method [19,20].

The flexoelectric polarization leads to the development of surface line charges along the crinkle valleys and ridges. The ridges are negatively charged, while the valleys are positively charged, to produce N-type and P-type crinkles respectively. The apparent line charges can cause preferential adsorption of molecules. A very striking manifestation of the line charges can be seen in adsorption of buckyballs along crinkle valleys in highly oriented pyrolytic graphite (HOPG). Buckyballs (C_{60}) are highly polarizable dielectric molecules. In the presence of strong enough external field, dielectrically polarized buckyballs are attracted to the field source. Figure 3*b*(i) shows buckyballs sprinkled over an HOPG surface. Instead of arranging themselves in clusters as the minimum energy state of buckyballs in absence of external electric field, they choose to align themselves in relatively long straight line segments with clear spacing and distinct directional preference to their arrangement [12]. A similar finding was previously reported in [18] (figure 3*b*(i) inset). In the higher resolution inset picture, we see that the inter-buckyball spacing is

approximately 2.5 nm. Here, we consider a simple model of a line charge that induces a dielectric dipole in every buckyball and aligns the electrically polarized buckyballs with a spacing distance l. The dipole arm length is denoted d, and the distance between the buckyball and the line charge h as shown in figure 3*b*(ii). The dipoles are attracted to the line charge of the crinkle valleys or ridges by the electric field gradient. The attraction potential per unit length of the line charge is inversely proportional to the inter-spacing distance l. This apparent aggregation attraction is balanced with inter-dipole repulsions. Expression of the net buckyball-interaction potential is derived in appendix A. Figure 3*b*(iii) shows a plot for the potential energy as a function of the spacing l. The energy minimum is attained at $l \approx 2$ nm with rough estimations of h and d, which is in relatively close agreement with the experimental observation. Thus, the alignment of buckyballs on the HOPG surface can be explained by the existence of crinkles and the resulting flexoelectric surface-charge concentrations along the valleys and ridges. Our simulation shows the alignment of the buckyballs along the valleys of the crinkles is more stable than along the ridges. In addition, we analysed adsorption potentials of H_2 and O_2 molecules with DFT. The adsorption potentials of H_2 and O_2 increase approximately 20 eV and approximately 30 eV at the crinkle ridge, respectively, which represents 11–12% increase over the adsorption on a flat HOPG surface.

5. Discussion

(a) From non-local model to reduced models

Having established the mathematical formalism for the non-local model, we employ this development to concretely derive the two reduced models discussed in §2 from this general model.

We first consider a uniformly bent single layer of graphene. The curvature is assumed to be small enough that the layer can be assumed straight for calculation purposes. From the symmetry of the problem and assuming $L_0 \gg r_0$, polarization density of the single layer, $\overset{\vee}{P}_{(1)}$, is constant everywhere. Under these assumptions, equation (3.3) reduces to

$$\overset{\vee}{E}(s) = \int_{-L_0}^{L_0} \overset{\vee}{P}_{(1)}(s') g_{(1)}(s - s')\, \mathrm{d}s', \tag{5.1}$$

where $g_{(1)}(s - s') = -1/2\pi\epsilon_{(1)} q_1(s, s')/\{(x(s) - x(s'))^2\}$. Performing the integration, we get that $\overset{\vee}{E}_{(1)} = -\overset{\vee}{P}_{(1)}/(\pi\epsilon_{(1)} r_0)$ where r_0 is the cut-off radius. Plugging back into the constitutive relation and simplifying we get the linear operator $\mathcal{L}_2[\overset{\vee}{P}_{(1)}] = \{1 + \alpha/(\pi\epsilon_{(1)} r_0)\}\overset{\vee}{P}_{(1)}$. In other words,

$$\overset{\vee}{P}_{(1)} = \beta_{(1)}^{(\mathrm{uc})} \kappa = \frac{\beta_{(1)}^{(\mathrm{in})} \kappa}{1 + \alpha/(\pi\epsilon_{(1)} r_0)}. \tag{5.2}$$

The coefficient, $\beta_{(1)}^{(\mathrm{in})}/\{1 + \alpha/(\pi\epsilon_{(1)} r_0)\}$, is referred to as the 'flexoelectric constant' in Kalinin & Meunier [13]. Note that in the current study, the intrinsic flexoelectric constant for single-layer graphene is not known. However, the above equation provides a way to evaluate $\beta_{(1)}^{(\mathrm{in})} \cong 0.16\mathrm{e}$ for $\beta_{(1)}^{(\mathrm{uc})} \cong 0.11\mathrm{e}$. The uniform curvature limit, thus leads to a very simplified dependence of electric field on the polarization and this allows the reduction of the $\mathcal{L}_2$ linear operation to just a pre-factor. The reduction in $\beta^{(uc)}$ value as compared to the intrinsic flexoelectric constant is due to the weakening effect of dielectric polarization on intrinsic polarization as discussed in §2b.

For a highly localized curvature distribution like the crinkle, we expect that the general model also reduces to an e-local model approximately. To this end, we design a calibration test for computational brevity. We choose the following function to represent the crinkle curvature distribution.

$$\kappa_{\mathrm{test}}(x; \lambda) = \kappa_0 \cos kx e^{-akx}, \tag{5.3}$$

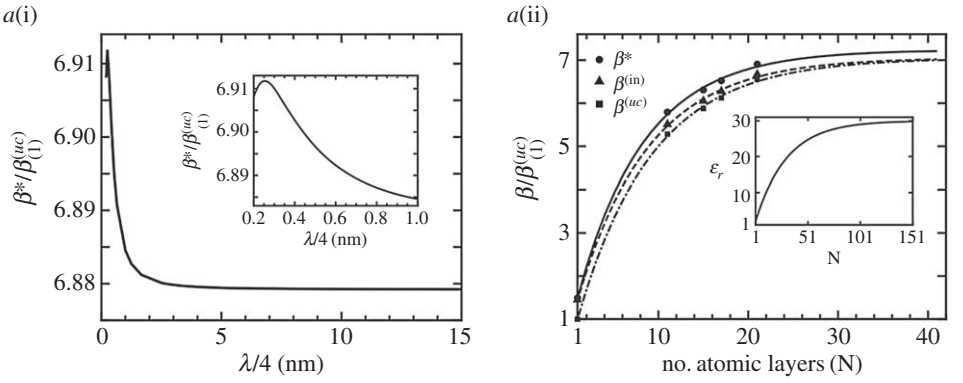

Figure 4. (*a*(i)) Calibration curve for β^* as function of wavelength; (ii) Evolution of the flexoelectric coefficients and relative permittivity with the number of layers *N*.

with $k = 2\pi/\lambda$, for a parameter λ, as it resembles the curvature distribution of the crinkle—highly localized and oscillatory. The peak curvature, period and decay length of the test-function can be tuned independently. In this calculation, we calibrate the peak curvature κ_0, the wavelength λ and the decay-length parameter a of a test-function to match the peak curvature of the 3° crinkle. From the curvature distribution and employing equation (3.3), we calculate the net polarization. In the e-local approximation, the net polarization and curvature are proportional and related by the effective flexoelectric constant. Denoting the ratio of the calculated peak polarization and peak curvature by β^*, we plot the results in figure 4*a*(i) as a function of the wavelength λ of the test-function. The results are shown for a 21-layered, 15 nm long MLG specimen. Results show, that for test-function with the same wavelength as the crinkle curvature distribution i.e. $\lambda/4 \sim 0.6$ nm, the effective flexoelectric constant is $\sim 6.89\beta^{(\mathrm{uc})}_{(1)}$. This is in agreement with the e-local model. The results indicate that e-local model, obtained as a limiting case of the general model with flexoelectricity–dielectricity coupling, is a good approximation. We note that the figure 4*a*(i) remains insensitive to the amplitude of the test-function and thus is a universal calibration curve for any crinkle angle.

The oscillatory nature of the curvature distribution enhances the intrinsic flexoelectric polarization by augmenting it with the dielectric polarization. The invariance in the shape of distribution, as discussed in [1] ensures that the polarization and curvature scale linearly with the end angle (figure 2*a*(i,ii)), thereby reducing equation (1.8) to the e-local model,

$$\overset{\vee}{P} = \beta^* \kappa. \tag{5.4}$$

(b) Layer dependence of properties

The dielectric properties of graphene are known to be dependent on the number of layers and the location of the layer in MLG. The microscopic picture of electrical interactions in the layers is sensitive to the number of layers and the location, and thus the dielectric and flexoelectric properties over the number of layers are layer-number dependent. Regarding dielectric properties of few layer graphene, Santos *et al.* [21] showed with DFT analysis that relative permittivity increases nearly linearly with the electric field for small electric fields. Hotta *et al*. [22] report that the bulk relative permittivity, ϵ_r, of graphite is approximately 30. Figure 4*a*(ii) inset shows an exponential interpolation of the relative permittivity, $\epsilon_{r(N)} = \epsilon_{r(1)} + (\epsilon_{r(\infty)} - \epsilon_{r(1)})\{1 - e^{-S(N-1)/(\epsilon_{r(\infty)} - \epsilon_{r(1)})}\}$, with $S = d\epsilon_{r(N)}/dN$ at $N = 1$, that depends on the number of layer N, and fits both the few layer and bulk limit. Now, our interest is in flexoelectric coefficients that depend on the number of layers. Qualitatively, increasing the number of layers raises attractive interlayer interactions that lower the potential energy in the crinkle morphology.

Thus, the effective flexoelectric coefficient should increase. Similarly, the interlayer attractive interaction intensifies with an increasing number of layers for uniformly curved MLG as well, and the uniform curvature flexoelectric coefficient is also expected to increase. To calculate the layer-number-dependent behaviour of flexoelectric coefficients, we first evaluate the intrinsic flexoelectric coefficient, $\beta^{(\mathrm{in})}_{(N)}$, for various number of layers by iterating the coefficient value until the peak curvature of the non-local model matches that obtained by the DFT analysis for a 3° end angle case. The coefficient $\beta^{(\mathrm{in})}_{(N)}$ is shown in figure 4*a*(ii). Once we have the intrinsic flexoelectric constant, we evaluate $\mathcal{L}_2$ in (3.4) for uniform curvature distribution to obtain the uc-local flexoelectric coefficient $\beta^{(\mathrm{uc})}_{(N)}$. Figure 4*a*(ii) shows that the coefficient $\beta^{(\mathrm{uc})}_{(N)}$ also increases with the number of layers and saturates to a bulk value. Lastly, the e-local flexoelectric coefficient, $\beta^{*}_{(N)}$, can be simply obtained by the ratio of the peak polarization to the peak curvature. The coefficient $\beta^{*}_{(N)}$ increases with the number of layers and saturates to a bulk value. As discussed in §2b, we find that $\beta^{*} > \beta^{(\mathrm{in})} > \beta^{(\mathrm{uc})}$. In summary, our fitting yields the following expressions for flexoelectric coefficients: $\beta^{*}_{(N)} = 7.235 - 6.841e^{-0.1377N}$; $\beta^{(\mathrm{in})}_{(N)} = 7.052 - 6.357e^{-0.1266N}$; $\beta^{(\mathrm{uc})}_{(N)} = 7.046 - 6.817e^{-0.1205N}$; $\varepsilon_{r(N)} = 30 - 28.8594e^{-0.0333N}$.

6. Conclusion

1. We investigate the thermodynamically motivated constitutive law for flexoelectricity in graphene. The coupling of dielectricity and flexoelectricity is quantitatively analysed with the thermodynamic framework, while the coupling mechanisms are qualitatively elucidated. We unify the framework for the existing disparate models in uniform curvature and highly localized regimes.
2. We propose a mathematical formulation for modelling electromechanics in two-dimensional layered materials. While the existing approach in the literature predominantly employs Maxwell's electric field-based continuum framework, we apply Legendre transformation of the Maxwell's free-energy potential to another polarization-based one that allows us to construct a free-energy potential for two-dimensional layered materials. Our energetic modelling of the two-dimensional materials with the transformed potential provides computational advantages where the problem can be reduced from solving field quantities for entire space to analysing non-local polarization interactions just over the layers.
3. The non-local model applied to 21 layer, 15 nm span graphene sample produces highly localized curvature distribution, a signature of the crinkle mode of buckling. These results are in close agreement with DFT and e-local model predictions. The curvature focusing band width is found to be approximately 0.86 nm.
4. We observe notable effects of constitutive non-locality in non-uniform curvature and polarization distributions. In crinkles, the coupling enhances curvature reversal, consequently amplifying the polarization reversal as well. The e-local model lumps this constitutive non-locality into one single parameter and therefore misses out on this detail.
5. The flexoelectric polarization near the crinkle ridge, predicted by our non-local model, is found to match with DFT results. The manifestation of flexoelectric crinkle charges is observed in the form of buckyballs aligning in a straight line on an HOPG surface. Our simplified model of buckyball adsorption along a line charge is able to capture the underlying physics of the process. We believe that crinkle polarization is a significant outcome which can have far reaching implications in manipulating charged and polarizable molecules.
6. Our DFT analysis shows that enhancement in adsorption of neutral molecules at crinkle ridges depends on the molecular weight and possibly geometry of the molecule as well. The change of physical binding energy of H_2 and O_2 molecules on the crinkle surface is found to be approximately 20 eV and approximately 30 eV respectively, which is approximately 11–12% of the total binding energy.

7. We show that the non-local model is reducible to the uc-local and the e-local models [1]. Our calibration test reveals that the e-local model is accurate enough when the curvature is highly localized like in crinkles, while the uc-local is exact in the limit of uniform curvature distribution.
8. We investigate the layer-number dependence of flexoelectric coefficients and find that the flexoelectric coefficients increase with number of layers and saturate to a bulk value.
9. For an experimental verification of our analytical results, measurement of the approximately 1 nm band width of the crinkle ridge is non-trivial due to the localized surface line charge; however, we could measure the width down to 1.76 nm with an atomic lattice interferometry [23]. For another experimental verification, the electric line charge could be indirectly revealed by linear adsorption of buckyballs as cited in figure 3*b*(i) [12]. It would be desirable to directly measure the line charge density within approximately 1 nm band width with further improvements in resolution of currently available experimental techniques.
10. The flexoelectricity–dielectricity coupling in graphene crinkles can selectively adsorb charged or polarizable molecules in a linear array, and the adsorption characteristics can be developed as a strain-controlled 'molecular zipper'. In addition, as fractional stacking shift and twist [24] of two-dimensional material layers are considered to provide diverse electronic and optical properties, mechanics of crinkles is expected to provide means to study novel properties of stacking-controlled two-dimensional materials.

Data accessibility. This article has no additional data.

Authors' contributions. M.K. and K.-S.K. conceived and implemented the mathematical model, interpreted the results and drafted the manuscript. M.-H.C. and K.S.K. carried out the DFT analysis. M.K., V.L. and K.-S.K. formulated the thermodynamic framework. K.-S.K. supervised the work. All authors gave final approval for the publication.

Competing interests. We declare we have no competing interests.

Funding. This work was supported by the U.S. National Science Foundation (Awards CMMI-1462785 and 1563591) for the experimental study and the theoretical modelling by M.K. and K.-S.K. and (Awards DMR-0520651 and XSEDE) for the DFT analysis by M.-H.C. and K.-S.K. V.L. was supported by the Hibbitt Fellowship at Brown University.

Acknowledgements. Valuable discussions with Dr Ruizhi Li on graphene crinkle and buckyball experiments are gratefully acknowledged.

Appendix A. Inter C_{60} spacing on crinkle ridge

The potential energy of the buckyballs on a crinkle ridge or valley (figure 3*b*(ii)) per unit spacing can be formulated as,

$$\psi(l) = \frac{1}{4\pi\epsilon l}\left\{Qq\int_{-\infty}^{\infty}\frac{1}{\sqrt{(h+d)^2+x^2}} - \frac{1}{\sqrt{h^2+x^2}}\right\}\mathrm{d}x + \frac{1}{4\pi\epsilon l}2Q^2\sum_{i=1}^{\infty}\left(\frac{1}{il} - \frac{1}{\sqrt{d^2+i^2l^2}}\right). \quad \text{(A 1)}$$

Simplifying (A 1) gives

$$\frac{\Phi(l)}{Q^2} = \frac{4\pi\epsilon\psi(l)}{Q^2} = \frac{-2q/Q}{l}\ln\frac{(h+d)}{h} + \frac{2}{l^2}\sum_{i=1}^{\infty}\frac{1}{i}\left(1 - \frac{1}{\sqrt{(d/il)^2+1}}\right). \quad \text{(A 2)}$$

The function $\Phi(l)$ can now be minimized to find the optimal inter-buckyball spacing. We assume $qd/Q = 0.5$, $h = d = 1\ nm$ for this calculation, and $\Phi(l)$ is plotted in figure 3*b*(iii).

References

1. Kothari M, Cha M-H, Kim K-S. 2018 Critical curvature localization in graphene. I. Quantum-flexoelectricity effect. *Proc. R. Soc. A* **474**, 20180054. (doi:10.1098/rspa.2018.0054)

2. Dhanabalan SC, Ponraj JS, Zhang H, Bao Q. 2016 Present perspectives of broadband photodetectors based on nanobelts, nanoribbons, nanosheets and the emerging 2D materials. *Nanoscale* **8**, 6410–6434. (doi:10.1039/c5nr09111j)
3. Ying Y, Yang Y, Ying W, Peng X. 2016 Two-dimensional materials for novel liquid separation membranes. *Nanotechnology* **27**, 332001. (doi:10.1088/0957-4484/27/33/332001)
4. Mashkevich VS. 1957 Electrical, optical, and elastic properties of diamond-type crystals II. Lattice vibrations with calculation of atomic dipole moments. *Sov. Phys. J. Exp. Theor. Phys.* **5**, 707–713.
5. Kogan SM. 1964 Piezoelectric effect during inhomogeneous deformation and acoustic scattering of carriers in crystals. *Sov. Phys. Solid State* **5**, 2069–2070.
6. Mohammadi P, Liu LP, Sharma P. 2013 A theory of flexoelectric membranes and effective properties of heterogeneous membranes. *J. Appl. Mech.* **81**, 11007. (doi:10.1115/1.4023978)
7. Liu LP, Sharma P. 2013 Flexoelectricity and thermal fluctuations of lipid bilayer membranes: renormalization of flexoelectric, dielectric, and elastic properties. *Phys. Rev. E* **87**, 032715. (doi:10.1103/physreve.87.032715)
8. Liu L. 2013 On energy formulations of electrostatics for continuum media. *J. Mech. Phys. Solids* **61**, 968–990. (doi:10.1016/j.jmps.2012.12.007)
9. Liu L. 2014 An energy formulation of continuum magneto-electro-elasticity with applications. *J. Mech. Phys. Solids* **63**, 451–480. (doi:10.1016/j.jmps.2013.08.001)
10. Courant R, Hilbert D. 1962 *Methods of mathematical physics*, vol. II, pp. 32–39. New York, NY: Interscience.
11. Toupin RA. 1956 The elastic dielectric. *J. Ration. Mech. Anal.* **5**, 849–915. (doi:10.1512/iumj.1956.5.55033)
12. Li R, Kothari M, Landauer AK, Cha M-H, Kwon H, Kim K-S. 2018 A new subcritical nanostructure of graphene—Crinkle-Ruga structure and its novel properties. *MRS Adv.* **3**, 2763–2769. (doi:10.1557/adv.2018.432)
13. Kalinin SV, Meunier V. 2008 Electronic flexoelectricity in low-dimensional systems. *Phys. Rev. B* **77**, 033403. (doi:10.1103/physrevb.77.033403)
14. Jung JH, Bae J, Moon M-W, Kim K-S, Ihm J. 2015 Numerical study on sequential perioddoubling bifurcations of graphene wrinkles on a soft substrate. *Solid State Commun.* **222**, 14–17. (doi:10.1016/j.ssc.2015.08.020)
15. Shabalin IL. 2014 Carbon (graphene/graphite). In *Ultra-high temperature materials I*, p. 69. Amsterdam, The Netherlands: Springer.
16. Ho TA, Striolo A. 2013 Polarizability effects in molecular dynamics simulations of the graphene-water interface. *J. Chem. Phys.* **138**, 54117. (doi:10.1063/1.4789583)
17. Langlet R, Devel M, Lambin P. 2006 Computation of the static polarizabilities of multi-wall carbon nanotubes and fullerites using a Gaussian regularized point dipole interaction model. *Carbon* **44**, 2883–2895. (doi:10.1016/j.carbon.2006.05.050)
18. Klitgaard SK, Egeblad K, Haahr LT, Hansen MK, Hansen D, Svagin J, Christensen CH. 2007 Self-assembly of C60 into highly ordered chain-like structures on HOPG observed at ambient conditions. *Surf. Sci.* **601**, L35–L38. (doi:10.1016/j.susc.2007.03.022)
19. Bader RFW. 1991 A quantum theory of molecular structure and its applications. *Chem. Rev.* **91**, 893–928. (doi:10.1021/cr00005a013)
20. Henkelman G, Arnaldsson A, Jónsson H. 2006 A fast and robust algorithm for Bader decomposition of charge density. *Comput. Mater. Sci.* **36**, 354–360. (doi:10.1016/j.commatsci.2005.04.010)
21. Santos EJG, Kaxiras E. 2013 Electric-field dependence of the effective dielectric constant in graphene. *Nano Lett.* **13**, 898–902. (doi:10.1021/nl303611v)
22. Hotta M, Hayashi M, Lanagan MT, Agrawal DK, Nagata K. 2011 Complex permittivity of graphite, carbon black and coal powders in the ranges of X-band frequencies (8.2 to 12.4 GHz) and between 1 and 10 GHz. *ISIJ Int.* **51**, 1766–1772. (doi:10.2355/isijinternational.51.1766)
23. Jang BK, Kim J, Lee HJ, Kim K, Wang C. 2015 'Device and method for measuring distribution of atomic resolution deformation,' United States Patent, Patent Number 9,003,561: issued on April 7, 2015.
24. Cao Y, Fatemi V, Fang S, Watanabe K, Taniguchi T, Kaxiras E, Jarillo-Herrero P. 2018 Unconventional superconductivity in magic-angle graphene superlattices. *Nature* **556**, 43–50. (doi:10.1038/nature26160)